Materials Horizons

ROYAL SOCIETY OF CHEMISTRY

COMMUNICATION

View Article Online
View Journal

Check for updates

Cite this: DOI: 10.1039/d5mh00858a

Received 7th May 2025,
Accepted 14th July 2025

DOI: 10.1039/d5mh00858a

rsc.li/materials-horizons

Hydrophilic sp^2-carbon conjugated co-porphyrin covalent organic frameworks for efficient electrocatalytic oxygen reduction reaction†

Yan-Fang Yao,[a] Yun-Rui Lv,[a] Feng Li,[a] Xin-Yi Huang,[a] Si-Jing Huang,*[b] Xin-Yan Xiao *[a] and Hai-Yang Liu *[a]

Covalent organic frameworks (COFs) have demonstrated great potential in electrocatalytic oxygen reduction reaction (ORR). However, the continuous proton-coupled electron transfer (PCET) steps with water as the proton donor and the low electron conductivity of hydrophobic COFs increase the kinetic barriers for device applications. Herein, a hydrophilic custom-designed strong electron/proton extractor on CoT-sp^{2}C-P-COF-COOH was developed by converting the cyano groups of CoT-sp^{2}C-P-COF into carboxyl groups. The electrocatalyst constructed by the CoT-sp^{2}C-P-COF-COOH shows impressive ORR activity ($E_{1/2}$ = 0.823 V *vs.* RHE) and outperforms most COF-based catalysts. Additionally, the fabricated Zn–air battery with the CoT-sp^{2}C-P-COF-COOH catalyst displays a high peak power density of 121.8 mW cm^{-2} and excellent stability. Theoretical calculations suggest that CoT-sp^{2}C-P-COF-COOH is also more efficient than CoT-sp^{2}C-P-COF to bind with an O_2 molecule to form $Co^{III}–O_2^{\bullet-}$, which optimizes the electron transfer efficiency and enhances the stabilization of intermediates, thereby synergistically accelerating the PCET step and ORR kinetics. This work highlights the continuous electron extraction and rapid proton transfer during electrocatalysis, and paves the way for advances in designing hydrophilic ORR electrocatalysts at the molecular level.

New concepts

This work introduces a novel approach to enhancing the electrocatalytic performance of covalent organic frameworks (COFs) for oxygen reduction reaction (ORR) by functionalizing them with hydrophilic strong electron/proton extractors. By converting cyano groups to carboxyl groups in CoT-sp^{2}C-P-COF, a highly active and stable ORR electrocatalyst, CoT-sp^{2}C-P-COF-COOH, with impressive performance was developed, including an $E_{1/2}$ of 0.823 V *vs.* RHE and a peak power density of 121.8 mW cm^{-2} in a Zn–air battery. Theoretical calculations reveal that this modification optimizes electron transfer efficiency and stabilizes reaction intermediates, thereby accelerating proton-coupled electron transfer (PCET) steps. This study highlights the importance of continuous electron extraction and rapid proton transfer in electrocatalysis, providing a new strategy for designing hydrophilic ORR electrocatalysts at the molecular level.

1. Introduction

Efficient electrocatalytic small gas molecules driven by renewable energy play a crucial role in the development of clean electrochemical energy conversion technologies.[1–4]

Among of them, the oxygen–water oxygen reduction reaction (ORR) relies on water as a source of protons and electrons, thus limiting the energy and power densities.[4–6] Moreover, the low solubility of oxygen in water largely restricts the current density that can be achieved by liquid-phase electrocatalytic technologies such as fuel cells and zinc–air batteries.[7,8] From a molecular mechanism perspective, the ORR involves two essential proton-coupled electron transfer (PCET) steps, highlighting the critical interdependence between sustained electron transport dynamics and adequate proton supply.[9–12] As described by the Grotthuss mechanism, proton transfer in aqueous environments occurs through a water–hydronium network.[11,13,14] Therefore, hydrophilic ligands such as oxygen-containing functional groups on material surfaces are crucial for optimizing proton transfer efficiency.

Covalent organic frameworks (COFs), as an emerging class of crystalline porous organic polymer, have rapidly become promising materials for photoelectrocatalysis attributed to their exceptional surface area, precisely engineered active sites, and robust framework integrity.[15–21] Furthermore, COFs are also structurally designable, allowing the modulation of the active sites, electronic structures, and pore environments, which is advantageous for improving electrocatalysis performance.[5,16,22–24] In particular, a variety of organic ligands and conjugated backbones can also be used to manipulate their electronic structure to improve

---

[a] School of Chemistry and Chemical Engineering, Guangdong Provincial Key Laboratory of Fuel Cell Technology, South China University of Technology, Guangzhou 510641, China. E-mail: cexyxiao@scut.edu.cn, chhyliu@scut.edu.cn

[b] Analytical and Testing Center, South China University of Technology, Guangzhou 510641, China. E-mail: hsjscut@scut.edu.cn

† Electronic supplementary information (ESI) available. See DOI: https://doi.org/10.1039/d5mh00858a

electrochemical performance.[25–27] Porphyrins and its metallized derivatives have been widely used as small molecule electrocatalytic centers due to their unique transition metal–nitrogen–carbon structures.[28–31] Moreover, their easily modifiable macrocyclic structure allows them to be embedded in crystalline porous materials such as metal–organic frameworks (MOFs) and COFs, making them catalyst candidates of great interest.[32–34] In 2017, the Co-porphyrin-based COF was first used in catalyzing the ORR.[35] Afterwards, several COF-based electrocatalysts have been synthesized and applied for the ORR.[36–40] For example, precisely engineered 1D ion-conductive nanochannels were strategically constructed within cobalt-incorporated COFs, enabling efficient hydroxyl ion migration through their crystalline porous architecture.[5] Heteroatoms (N, S) were integrated into the Co-porphyrin-based COFs to achieve the spacing of the active sites.[26] A high-efficiency COF with Co–N–C structures was constructed using molecular units to constrain charge behaviors.[22] More recently, two-dimensional porphyrin-based COFs with pentagonal pores were developed by rationally combining C_4 and C_2 symmetric building blocks into mcm networks.[41] Hence, metalloporphyrin-based COFs are a promising alternative material for the ORR, owing to the high-efficiency active M–N_4 sites and the outstanding chemical stability. However, the insufficient charge transfer between the frameworks and mass transfer limitations caused by hydrophobic pores still pose challenges to the electrocatalytic performance of the ORR. Thus, designing hydrophilic COFs with strong charge and mass transfer capabilities is crucial for improving ORR activity.

The introduction of cyano groups into the framework allows for subsequent modification to carboxyl groups, making COFs a stronger electron/proton extractor with higher hydrophilicity and stronger dispersibility.[42–44] Furthermore, such structural engineering significantly improves its suitability for charge and proton conduction applications in electrocatalytic processes. In this study, we have first constructed a T-sp^{2}C-P-COF with a high density of cyano groups on its pore walls as the parent COF sample through a systematic screening of the reaction conditions (Table S1, ESI†). Subsequently, we coordinated this parent COF with cobalt ions to obtain the CoT-sp^{2}C-P-COF. After the modification treatment, the fully conjugated lefin-linked CoT-sp^{2}C-P-COF-COOH was synthesized, showing stronger hydrophilicity, more proton transport channels and higher charge-carrier separation efficiency (Scheme 1). As a result, all of these advantages result in CoT-sp^{2}C-P-COF-COOH ultimately providing promising ORR activity with a half-wave potential ($E_{1/2}$) of 0.823 V (*vs.* RHE), which is superior to most advanced COF-based ORR electrocatalysts.[5,26,45,46] Additionally, the zinc–air battery with CoT-sp^{2}C-P-COF-COOH displays a satisfactory 858 mAh g^{-1} specific capacity and 121.8 mW cm^{-2} power density. Theoretical calculations demonstrate that CoT-sp^{2}C-P-COF-COOH is also more efficient than CoT-sp^{2}C-P-COF to bind with an O_2 molecule to form Co^{III}–$O_2^{\bullet-}$. This work suggests the advantages of integrating Co-porphyrin and carboxyl groups in olefin-linked COFs for the rational design of efficient and stable ORR electrocatalysts.

2. Results and discussion

2.1. Structural characterization

Initially, the surface chemical compositions of the functionalized COFs materials were analyzed by Fourier transform-infrared (FT-IR) spectra (Fig. 1a). Compared with PDAN, the characteristic peaks of the C≡N bond stretching vibration of T-sp^{2}C-P-COF and CoT-sp^{2}C-P-COF were retained and red-shifted from 2249 cm^{-1} to 2216 cm^{-1}, which is due to the generation of the cyano-vinylene linkage (–C=C(C≡N)–), resulting in a larger conjugated system and thus improving the p-electron delocalization of the CN groups.[44] Due to the formation of conjugated C=C bonds (at 3030 cm^{-1}), the peak at 1698 cm^{-1} of the CHO of T-sp^{2}C-P-COF, CoT-sp^{2}C-P-COF and CoT-sp^{2}C-P-COF-COOH is greatly weakened compared to that of 4-CHO-TBPP. While the peak of the C≡N at 2216 cm^{-1} of T-sp^{2}C-P-COF and CoT-sp^{2}C-P-COF is well retained, offering an active site for post-modification. More importantly, the peak of the cyano group at 2249 cm^{-1} disappeared, and the emerging peaks at around 1670 and 1393 cm^{-1} were attributed to the stretching vibrations of the C=O bond and C–O bond from the carboxyl group of CoT-sp^{2}C-P-COF-COOH, indicating that the cyano group was successfully converted in CoT-sp^{2}C-P-COF.[47] Subsequently, the optical properties of the synthesized materials were investigated by ultraviolet-visible (UV-Vis) absorption spectra (Fig. 1b). The UV-vis spectrum of 4-CHO-TBPP exhibited

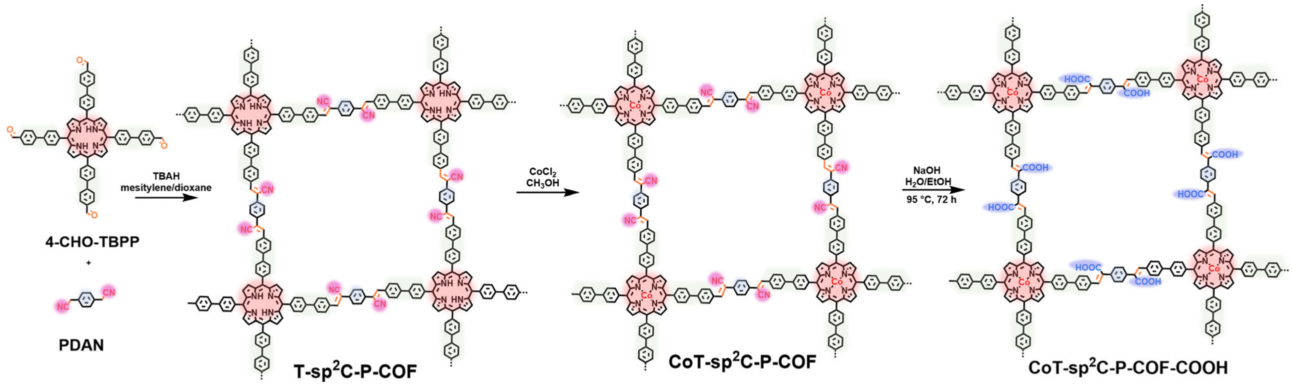

Scheme 1 Schematic of the synthesis strategy for T-sp^{2}C-P-COF, CoT-sp^{2}C-P-COF, and CoT-sp^{2}C-P-COF-COOH.

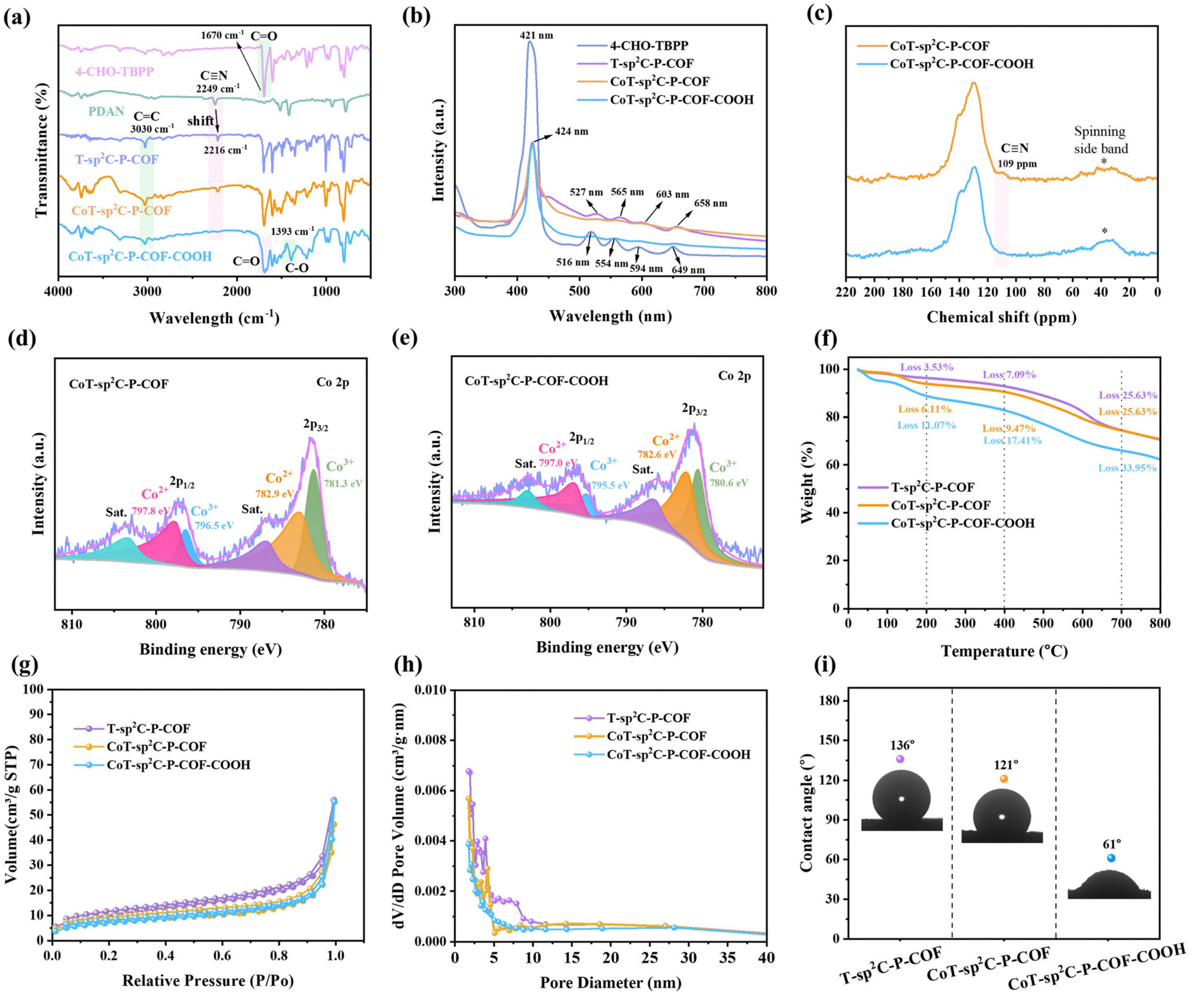

Fig. 1 (a) FTIR spectra of 4-CHO-TBPP, PDAN, T-sp^{2}C-P-COF, CoT-sp^{2}C-P-COF and CoT-sp^{2}C-P-COF-COOH. (b) UV-vis spectra of 4-CHO-TBPP, T-sp^{2}C-P-COF, CoT-sp^{2}C-P-COF and CoT-sp^{2}C-P-COF-COOH. (c) Solid-state ^{13}C NMR spectra of CoT-sp^{2}C-P-COF and CoT-sp^{2}C-P-COF-COOH. (d) and (e) Co 2p XPS results for CoT-sp^{2}C-P-COF and CoT-sp^{2}C-P-COF-COOH. (f) The thermos-gravimetric analysis of T-sp^{2}C-P-COF, CoT-sp^{2}C-P-COF and CoT-sp^{2}C-P-COF-COOH. (g) N_2 adsorption–desorption isotherms and (h) pore size distribution of T-sp^{2}C-P-COF, CoT-sp^{2}C-P-COF and CoT-sp^{2}C-P-COF-COOH. (i) The contact angles of T-sp^{2}C-P-COF, CoT-sp^{2}C-P-COF and CoT-sp^{2}C-P-COF-COOH.

a typical porphyrin Soret band at 421 nm and four weak Q bands at 516, 554, 594, and 649 nm due to the presence of uncoordinated porphyrin units. T-sp^{2}C-P-COF displayed a broadened Soret band at 424 nm along with significantly red-shifted Q bands at around 527, 565, 603 and 658 nm, possibly due to the presence of the large π-conjugated system in the COF skeleton. However, the absence of four Q bands was not observed in CoT-sp^{2}C-P-COF and CoT-sp^{2}C-P-COF-COOH, indicating successful coordination between the cobalt species and porphyrin units.[48] As shown in Fig. 1c, the chemical environment of CoT-sp^{2}C-P-COF and CoT-sp^{2}C-P-COF-COOH was characterized by cross-polarization magic-angle-spinning nuclear magnetic resonance (^{13}C CP-MAS NMR) spectra. In the ^{13}C CP-MAS NMR spectra of CoT-sp^{2}C-P-COF-COOH, the signal of C≡N disappeared at 109 ppm, which verified the successful conversion to the carboxyl group.[42] X-ray photoelectron spectroscopy (XPS) measurements revealed the existence of C and N in T-sp^{2}C-P-COF and CoT-sp^{2}C-P-COF, apart from this, new O signals occur in CoT-sp^{2}C-P-COF-COOH (Fig. S2 and S3, ESI†). Moreover, the Co 2p XPS spectra of CoT-sp^{2}C-P-COF and CoT-sp^{2}C-P-COF-COOH displayed that the peaks at binding energies of 781.3 eV and 796.5 eV are assigned to Co^{3+}, while the peaks at 782.9 eV and 797.8 eV are attributed to Co^{2+} (Fig. 1d and e). Two additional satellite peaks (marked as "Sat.") are located at 786.9 eV and 803.4 eV. The Co^{2+}/Co^{3+} ratio in CoT-sp^{2}C-P-COF-COOH, calculated based on the peak areas of Co^{3+} and Co^{2+}, is lower than that in CoT-sp^{2}C-P-COF. This may be due to the partial transfer of electrons from the cobalt porphyrin center to the benzoyl substituent through the electron-withdrawing effect of the –COOH groups. From the thermogravimetric analysis (TGA) curve shown in Fig. 1f, it can be observed that the weight loss process of the COF catalysts mainly consists of three stages under N_2 conditions. Before the temperature reaches 200 °C, the weight loss is less than 10%, which is mainly attributed to the removal of crystallization water and physically adsorbed water. In the temperature range of 200 to 400 °C, the weight loss is less than 20%. The weight retention rate of the synthesized COFs is over 70% within the range of 400 to 700 °C, indicating their excellent thermal stability, which can be attributed to the robustness of the sp^2 carbon bonds in the COF structure.[49,50] Among them, the thermal stability of the catalyst CoT-sp^2C-P-COF-COOH is slightly inferior to that of T-sp^2C-P-COF and CoT-sp^2C-P-COF. This may be due to the more fragile framework structure of CoT-sp^2C-P-COF-COOH, which could originate from its harsh post-treatment conditions.[42] The permanent porosities of all samples were measured by low-pressure N_2 adsorption measurements at 77 K (Fig. 1g, h and Fig. S4, ESI†). The Brunauer–Emmett–Teller (BET) surface areas of T-sp^2C-P-COF, CoT-sp^2C-P-COF, and CoT-sp^2C-P-COF-COOH were 37.03, 27.87, and 25.93 $m^2\ g^{-1}$, with corresponding average pore widths of 10.92, 12.67, and 17.00 nm, respectively. The low specific surface area (S_{BET}) is likely primarily attributed to the following factors: folding within the crystalline structure, which prevents some of the pores from being fully exposed; and the retention of solvent or substrate molecules within the pores, leading to blockages, a phenomenon that is consistent with some results reported in the literature.[51–53] In addition, the AB stacking mode hinders the orderly stacking of these COF layers, making it impossible for them to fully achieve porosity, and similar observations have also occurred in other AB stacked COFs.[54–56] The contact angles of T-sp^2C-P-COF, CoT-sp^2C-P-COF, and CoT-sp^2C-P-COF-COOH were measured to analyze their surface hydrophilicity. As shown in Fig. 1i, T-sp^2C-P-COF and CoT-sp^2C-P-COF were hydrophobic with contact angles as high as 136° and 121°, while CoT-sp^2C-P-COF-COOH showed good hydrophilicity with a smaller contact angle of 61°. The carboxylic acid group in CoT-sp^2C-P-COF-COOH creates a more hydrophilic surface, which will improve proton transfer, and the enhanced proton transfer stabilizes O_2 adsorption, indicating the presence of a potentially active site on the C atoms attached to the –COOH groups, which facilitates the electrocatalytic O_2 to H_2O process.[10,57,58]

The crystalline characteristics of the samples were evaluated by powder X-ray diffraction (PXRD) measurements (Fig. S5, ESI†). The diffraction patterns of T-sp^2C-P-COF (Fig. 2a), CoT-sp^2C-P-COF (Fig. 2b), and CoT-sp^2C-P-COF-COOH (Fig. 2c) all exhibit strong and sharp peaks at 2θ = 4.95°, which can be

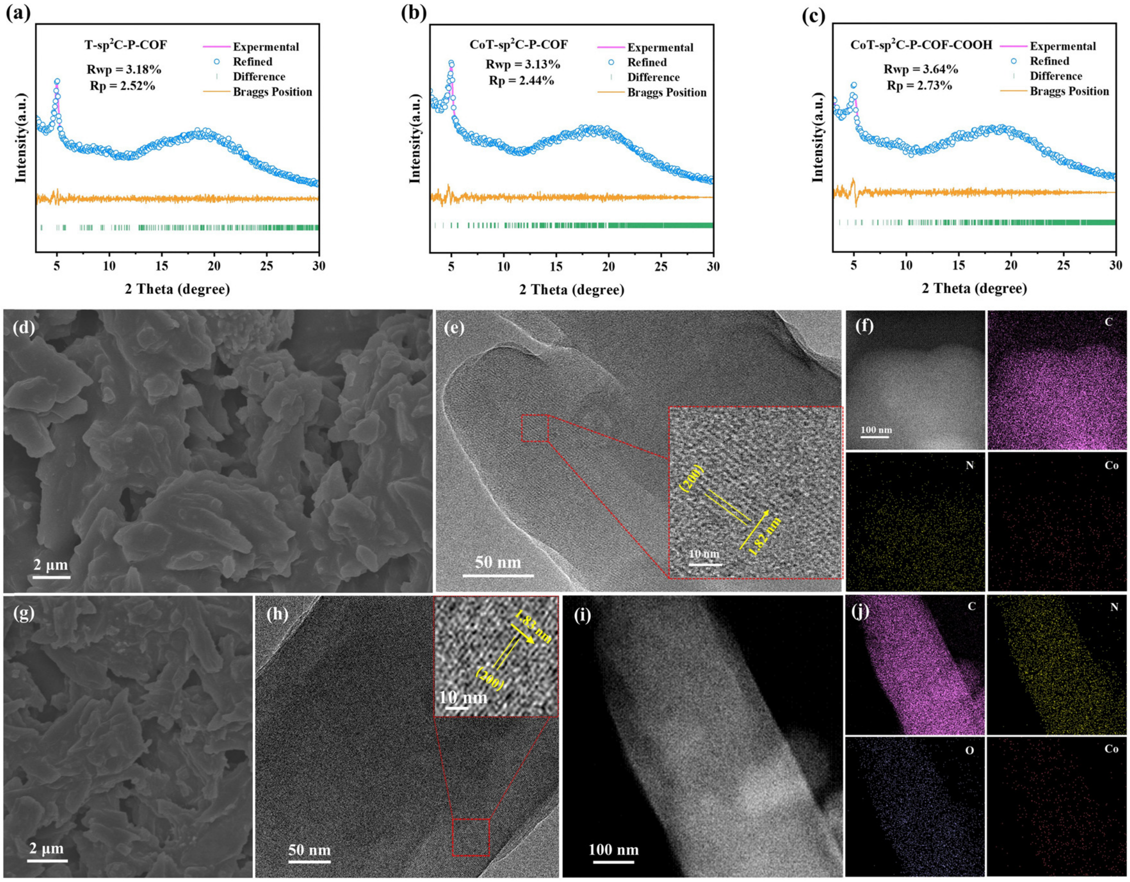

Fig. 2 PXRD patterns of (a) T-sp^2C-P-COF, (b) CoT-sp^2C-P-COF and (c) CoT-sp^2C-P-COF-COOH. (d) SEM, (e) TEM image, (f) HAADF-STEM image and EDS elemental mapping images of CoT-sp^2C-P-COF. (g) SEM, (h) TEM image, (i) HAADF-STEM image and (j) EDS elemental mapping images of CoT-sp^2C-P-COF-COOH.

attributed to the (200) plane, indicating high crystallinity. Pawley refinement analysis confirmed significant consistency between the calculated and experimental diffraction patterns. During the optimization process, the unit cell parameters of T-sp^{2}C-P-COF were determined to be: a = 34.49 Å, b = 34.48 Å, c = 3.62 Å, α = 90°, β = 90°, γ = 90°. For CoT-sp^{2}C-P-COF, the optimized unit cell parameters are: a = 34.66 Å, b = 34.59 Å, c = 3.79 Å, α = 90°, β = 90°, γ = 90°. The unit cell parameters of CoT-sp^{2}C-P-COF-COOH were optimized to: a = 34.50 Å, b = 34.44 Å, c = 3.79 Å, α = 90°, β = 90°, γ = 90°. Additionally, the refinement results showed low residual coefficients, with T-sp^{2}C-P-COF having an R_p value of 2.52% and an R_{wp} value of 3.18%; CoT-sp^{2}C-P-COF having an R_p value of 2.44% and an R_{wp} value of 3.13%; and CoT-sp^{2}C-P-COF-COOH having an R_p value of 2.73% and an R_{wp} value of 3.64%. These data demonstrate the consistency between the theoretical model and the experimental PXRD data. Among the diverse stacking modes, the AA stacking mode produces PXRD patterns that are consistent with the experimental profiles of the synthesized COFs (Fig. S6, ESI†). Moreover, among the various possible stacking configurations, the AB stacking mode is found to produce PXRD patterns that are in excellent agreement with the experimentally observed profiles of T-sp^{2}C-P-COF, CoT-sp^{2}C-P-COF and CoT-sp^{2}C-P-COF-COOH. As a result, all the COFs exhibit 2D skeletal structures with theoretical pore sizes of 1.87 nm, 1.89 nm, and 1.92 nm, respectively (Fig. S7, ESI†). The morphology and high crystal feature were characterized by scanning electron microscopy (SEM) and high-resolution transmission electron microscopy (HR-TEM) images. As shown in Fig. 2d and g, the SEM images of CoT-sp^{2}C-P-COF and CoT-sp^{2}C-P-COF-COOH exhibited no significant difference in the morphology, and both the COFs displayed uniform rod-shaped morphology. This observation confirmed that the cyano-to-carboxyl functional group interconversion within the COF skeleton cannot change the overall morphology. Furthermore, HR-TEM images of CoT-sp^{2}C-P-COF and CoT-sp^{2}C-P-COF-COOH show that the lattice spacings of CoT-sp^{2}C-P-COF and CoT-sp^{2}C-P-COF-COOH are 1.82 and 1.83 nm, respectively, both corresponding to 200 facets (Fig. 2e and h). Notably, the high-angle annular dark-field scanning TEM (HAADF-STEM) images and the corresponding energy-dispersive X-ray (EDX) elemental mapping images of CoT-sp^{2}C-P-COF and CoT-sp^{2}C-P-COF-COOH clearly showed that the elements in CoT-sp^{2}C-P-COF and CoT-sp^{2}C-P-COF-COOH are uniformly distributed (Fig. 2f, i and j).

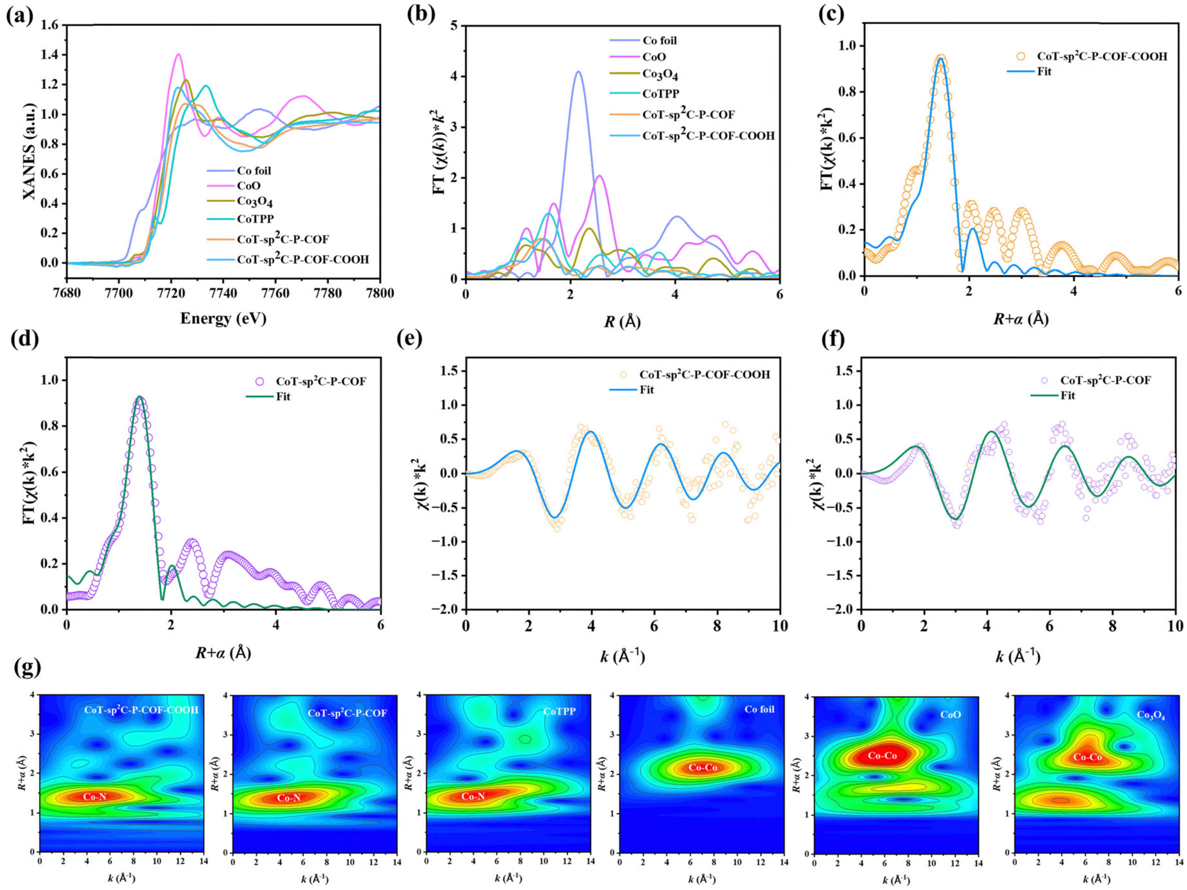

Fig. 3 (a) Normalized Co K-edge XANES spectra and (b) corresponding Fourier-transform EXAFS spectra of Co foil, CoO, Co_3O_4, CoTPP, CoT-sp^{2}C-P-COF and CoT-sp^{2}C-P-COF-COOH. (c) and (d) Co K-edge EXAFS and curve-fit in k^3-weight R-space and (e) and (f) corresponding k-space fitting curves for CoT-sp^{2}C-P-COF-COOH and CoT-sp^{2}C-P-COF. (g) Wavelet-transformed images for CoT-sp^{2}C-P-COF-COOH, CoT-sp^{2}C-P-COF, CoTPP, Co foil, CoO and Co_3O_4.

The Co K-edge X-ray absorption fine structure (XAFS) of CoT-sp^{2}C-P-COF and CoT-sp^{2}C-P-COF-COOH were employed to gain insight into the electronic structures and coordination topology of the cobalt centers. Fig. 3a illustrates that the X-ray absorption near-edge structure (XANES) spectra at the Co K-edge for both CoT-sp^{2}C-P-COF and CoT-sp^{2}C-P-COF-COOH exhibit a weak pre-edge peak at approximately 7706.3 eV and a shoulder peak at around 7712.4 eV, which are attributed to the 1s → 3d and 1s → $4p_z$ transitions, respectively. These findings indicate that the coordination environment of CoT-sp^{2}C-P-COF and CoT-sp^{2}C-P-COF-COOH is closer to that of CoTPP, in which Co atoms are coordinated with N to generate a Co–N_4 bond. The Fourier transform k^2-weighted extended X-ray absorption fine structure (EXAFS) at the Co K-edge for both CoT-sp^{2}C-P-COF and CoT-sp^{2}C-P-COF-COOH do not show any Co–Co signals, indicating the absence of Co clusters/particles in their frameworks (Fig. 3b). These results suggest that CMP-Py(Co) do not undergo Co aggregation during the metallization process, consistent with the HAADF-STEM results. Furthermore, CoT-sp^{2}C-P-COF and CoT-sp^{2}C-P-COF-COOH exhibit main peaks at 1.45 Å and 1.49 Å, which are attributed to the first Co–N shell. Besides, the calculated coordination number for the Co^{2+} ions in both CoT-sp^{2}C-P-COF and CoT-sp^{2}C-P-COF-COOH is 4 (Table S2, ESI†). Moreover, the EXAFS *R*-space and *k*-space fitting curve of CoT-sp^{2}C-P-COF and CoT-sp^{2}C-P-COF-COOH (Fig. 3c, e and d, f) and the fitted parameters summarized in Table S1 (ESI†) clearly revealing that the Co is coordinated to four N atoms (Co–N_4) with a bond distance of 1.97 Å. As illustrated in Fig. 3g, the wavelet transforms (WTs) of CoT-sp^{2}C-P-COF and CoT-sp^{2}C-P-COF-COOH display a prominent peak at approximately 4 Å^{-1}, which bears resemblance to that of CoTPP and can be ascribed to the Co–N coordination. Notably, no maximum intensity of Co–Co coordination was observed in both CoT-sp^{2}C-P-COF and CoT-sp^{2}C-P-COF-COOH

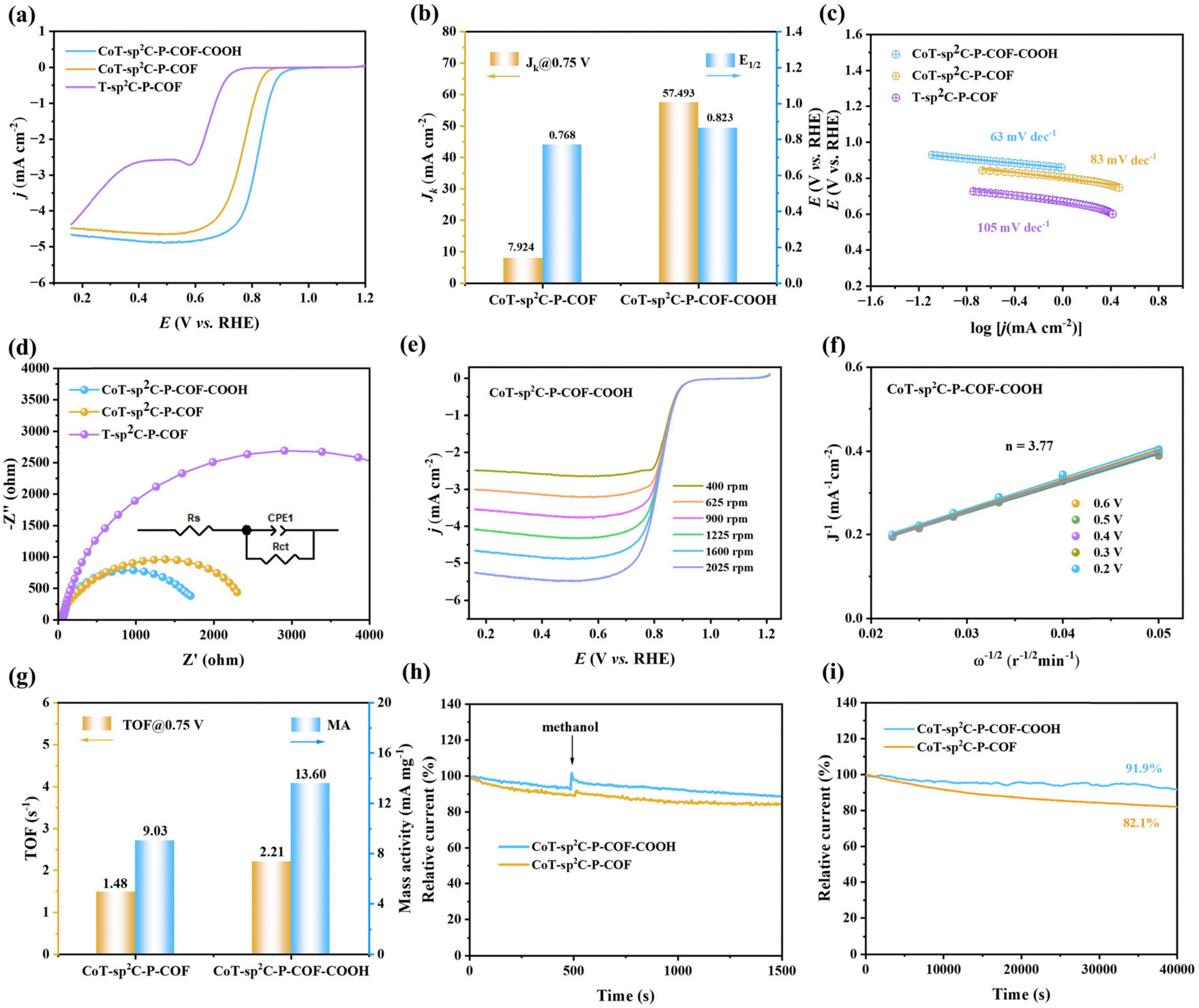

Fig. 4 (a) LSV curves of T-sp^{2}C-P-COF, CoT-sp^{2}C-P-COF and CoT-sp^{2}C-P-COF-COOH. (b) J_k (at 0.75 V *vs.* RHE) and $E_{1/2}$ of CoT-sp^{2}C-P-COF and CoT-sp^{2}C-P-COF-COOH. (c) Tafel plots of T-sp^{2}C-P-COF, CoT-sp^{2}C-P-COF and CoT-sp^{2}C-P-COF-COOH. (d) EIS plots of T-sp^{2}C-P-COF, CoT-sp^{2}C-P-COF and CoT-sp^{2}C-P-COF-COOH. (e) LSV curves of CoT-sp^{2}C-P-COF-COOH at different rotation speeds. (f) The corresponding K-L plots of CoT-sp^{2}C-P-COF-COOH. (g) TOFs and mass activity of T-sp^{2}C-P-COF, CoT-sp^{2}C-P-COF and CoT-sp^{2}C-P-COF-COOH. (h) Methanol tolerance tests of CoT-sp^{2}C-P-COF and CoT-sp^{2}C-P-COF-COOH. (i) Chronoamperometric responses for CoT-sp^{2}C-P-COF and CoT-sp^{2}C-P-COF-COOH.

compared to the WT contour maps of Co foils, confirming the absence of Co-derived crystalline structures in the frameworks.

2.2. Electrocatalytic performance

The oxygen reduction efficiency of the obtained COFs was evaluated by cyclic voltammetry (CV) and linear sweep voltammetry (LSV) polarization analyses using a three-electrode system in 0.1 M KOH electrolyte. The CV curves of all samples showed obvious cathodic peaks in O_2-saturated 0.1 M KOH solution, but no oxygen reduction peaks in N_2-saturated 0.1 M KOH solution. The cathodic peak potentials decreased in the order of CoT-sp^{2}C-P-COF-COOH > CoT-sp^{2}C-P-COF > T-sp^{2}C-P-COF, indicating that the presence of active site Co–N_4 and the formation of –COOH in the skeletons of the COFs had a great impact on the performance of the catalysts. Obviously, the peak potential of CoT-sp^{2}C-P-COF-COOH was the most positive, indicating that the ORR activity of CoT-sp^{2}C-P-COF-COOH was better compared with CoT-sp^{2}C-P-COF and T-sp^{2}C-P-COF (Fig. S8, ESI†). As depicted in Fig. 4a, the ORR activity of the samples was further confirmed by LSV curves in O_2-saturated 0.1 M KOH electrolyte at a scan rate of 1600 rpm. Obviously, with the metallization of the COFs and the generation of carboxyl groups, the performance of the COF catalysts was greatly enhanced with an impressive increase in half-wave ($E_{1/2}$) potential from 0.623 V to 0.823 V compared to that of the reversible hydrogen electrode (RHE). As shown in Fig. 4b, the optimized catalyst CoT-sp^{2}C-P-COF-COOH had an $E_{1/2}$ of 0.823 V and a calculated kinetic current density (J_k) of 57.493 mA cm^{-2} at 0.75 V, which is much higher than that of CoT-sp^{2}C-P-COF ($E_{1/2}$ = 0.768 V, J_k = 7.924 mA cm^{-2}) as well as the most well-reported COF catalysts and showed outstanding ORR activity (Table S3, ESI†). Additionally, Fig. 4a reveals that T-sp^{2}C-P-COF's LSV curve behaves unusually due to the lack of Co–N–C active sites, which are crucial for the efficient ORR.[59,60] These active sites assist in the adsorption and activation of oxygen and promote electron transfer. The –COOH groups in CoT-sp^{2}C-P-COF-COOH enhance hydrophilicity and proton transport, increasing the efficiency of PCET. Without these features, T-sp^{2}C-P-COF shows lower activity and poorer electron and proton transfer, leading to a shifted starting potential and weaker current response in its LSV curve. Furthermore, the Tafel slope of CoT-sp^{2}C-P-COF-COOH was calculated to be 63 mV dec^{-1}, which was much smaller than that of T-sp^{2}C-P-COF (105 mV dec^{-1}) and CoT-sp^{2}C-P-COF (83 mV dec^{-1}), validating the faster ORR kinetics of CoT-sp^{2}C-P-COF-COOH (Fig. 4c). As shown in Fig. 4d, the electrochemical impedance spectroscopy (EIS) Nyquist plot indicated that the charge transfer resistances of CoT-sp^{2}C-P-COF-COOH, CoT-sp^{2}C-P-COF, and T-sp^{2}C-P-COF were 1798, 2374, and 6083 Ω, respectively, revealing that CoT-sp^{2}C-P-COF-COOH had faster electron transfer ability. Based on the LSV curves recorded at various rotational speeds, the electron transfer number (n) of CoT-sp^{2}C-P-COF-COOH, CoT-sp^{2}C-P-COF, and T-sp^{2}C-P-COF, calculated from Koutecky–Levich (K–L) plots, was 3.77, 3.72, and 3.19, respectively, suggesting a 4e$^-$ pathway in the ORR process (Fig. 4e, f and Fig. S9, ESI†). The electrochemically active surface area (ECSA) was assessed by determining the electrochemical double-layer capacitance (C_{dl}) value using the CV method (Fig. S10, ESI†). As shown in Fig. S10d (ESI†), the C_{dl} for CoT-sp^{2}C-P-COF-COOH is 1.98 mF cm^{-2}, which is larger than that of T-sp^{2}C-P-COF (1.38 mF cm^{-2}) and CoT-sp^{2}C-P-COF (1.35 mF cm^{-2}), indicating that the CoT-sp^{2}C-P-COF-COOH can offer a more efficient active site. As shown in Fig. 4g, the turnover frequency (TOF) of the catalysts was estimated to compare the intrinsic activity of each active site. The TOF values of CoT-sp^{2}C-P-COF-COOH and CoT-sp^{2}C-P-COF were 2.21 and 1.48 s^{-1}, respectively These results indicated that CoT-sp^{2}C-P-COF-COOH exhibits the highest ORR catalytic activity among the acquired COFs, likely due to its carboxylic acid molecules forming a more hydrophilic surface, which improves proton transfer, with the enhanced proton transfer stabilizing O_2 adsorption and thereby facilitating the electrocatalytic conversion of O_2 to H_2O. Subsequently, chronoamperometric measurement was conducted to evaluate the stability of the CoT-sp^{2}C-P-COF-COOH. As depicted in Fig. 4h, the current density remained unchanged after the injection of 1.0 M methanol solution, suggesting the superior methanol resistance of CoT-sp^{2}C-P-COF and CoT-sp^{2}C-P-COF-COOH.

Significantly, the currents of the CoT-sp^{2}C-P-COF and CoT-sp^{2}C-P-COF-COOH catalysts were maintained at 82.1% and 91.9% of their initial currents after 40 000 s, respectively, demonstrating their outstanding stability (Fig. 4i). To assess the stability of CoT-sp^{2}C-P-COF-COOH after durability testing, FTIR was used to analyze the sample before and after the durability test. The spectra showed that the C=O and C–O peaks remained almost unchanged, confirming the robust chemical stability of the material (Fig. S11, ESI†). Furthermore, the XPS analysis revealed that the binding energies of C 1s, N 1s, O 1s, and Co 2p in CoT-sp^{2}C-P-COF-COOH remained virtually unchanged after durability testing, confirming that the chemical structure of CoT-sp^{2}C-P-COF-COOH was almost entirely preserved after the durability test (Fig. S12, ESI†). Moreover, SEM and TEM analyses showed that the structure of CoT-sp^{2}C-P-COF-COOH remained virtually unchanged after durability testing (Fig. S13, ESI†). These results collectively confirm that CoT-sp^{2}C-P-COF-COOH retains its structural integrity and exhibits good stability.

2.3. Zinc–air battery performance

Furthermore, to prove the practical application of hydrophilic COFs in energy storage devices, liquid zinc–air batteries (ZABs) were constructed (Fig. 5a). As illustrated in Fig. 5b, the open-circuit potential of the CoT-sp^{2}C-P-COF-COOH based ZAB was 1.49 V, which is slightly higher than that of the ZABs assembled by the CoT-sp^{2}C-P-COF (1.43 V). One ZAB using CoT-sp^{2}C-P-COF-COOH as the air cathode could uniformly power a light-emitting diode (LED) screen (Fig. 5b inset). The high peak power density of CoT-sp^{2}C-P-COF-COOH reaches up to 121.8 mW cm^{-2}, which is superior to the peak power density of the CoT-sp^{2}C-P-COF catalyst (101.2 mW cm^{-2}) in Fig. 5c. Moreover, the CoT-sp^{2}C-P-COF-COOH based ZAB displayed a specific capacity of 858 mAh g^{-1} at 10 mA cm^{-2}, surpassing those of the hydrophobic CoT-sp^{2}C-P-COF (798 mAh g^{-1}) catalyst assembled

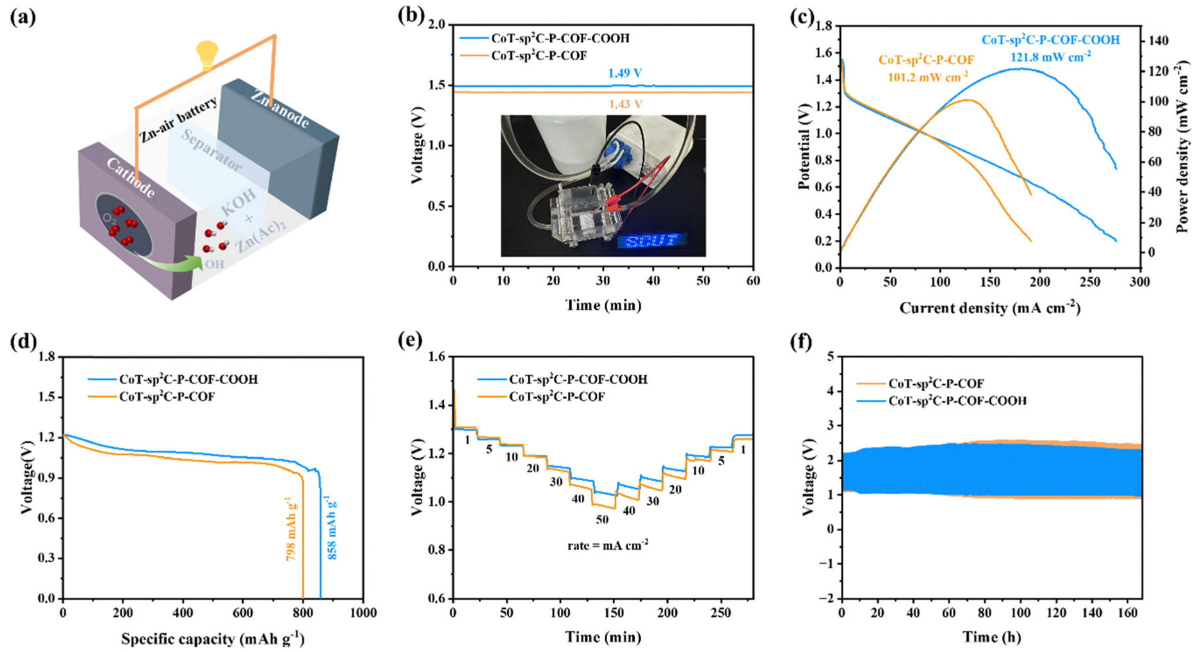

Fig. 5 Electrochemical performance of CoT-sp^{2}C-P-COF-COOH-based and CoT-sp^{2}C-P-COF-based ZABs. (a) Schematic construction of the aqueous ZAB. (b) Open-circuit potential plots. (c) Polarization and power density curves. (d) Specific capacities at 10 mA cm^{-2}. (e) The discharge curves at different current densities. (f) Long-term charge/discharge cycling curves at 10 mA cm^{-2}.

battery (Fig. 5d). Notably, as the discharge current density varies (1 → 50 mA cm^{-2}), the CoT-sp^{2}C-P-COF-COOH based ZAB maintained a higher sustained voltage plateaus than the CoT-sp^{2}C-P-COF catalyst constructed battery, particularly at higher current densities. Moreover, when the current density is restored to 1 mA cm^{-2}, the discharge voltage quickly restitutes, highlighting its excellent rate capability and reversible property (Fig. 5e). Remarkably, the rechargeable performance of the CoT-sp^{2}C-P-COF-COOH based ZAB was assessed and is shown in Fig. 5f. As expected, the CoT-sp^{2}C-P-COF-COOH based ZAB exhibited an excellent durability, with only an insignificant increase in voltage gap after 400 cycles over 170 h at the current density of 10 mA cm^{-2}. The aforementioned results suggest that CoT-sp^{2}C-P-COF-COOH is a superior replacement for noble-metal-based electrocatalysts, showcasing its enormous potential in advanced energy storage and conversion technologies.

2.4. Theoretical calculation

Additionally, the ORR processes associated with CoT-sp^{2}C-P-COF and CoT-sp^{2}C-P-COF-COOH were studied using DFT calculations. According to the configurations of the two model catalysts, Fig. 6a and b illustrate the 4e$^-$ ORR process mechanism after optimization of the structure of the adsorbed intermediates (*OOH, *O, and *OH) by CoT-sp^{2}C-P-COF-COOH and CoT-sp^{2}C-P-COF. The density of states (DOS) displayed that the CoT-sp^{2}C-P-COF-COOH shows a smaller bandgap near the Fermi level compared to the CoT-sp^{2}C-P-COF, suggesting that the modulation of the carboxyl functional group imparts superior semiconducting properties of CoT-sp^{2}C-P-COF-COOH (Fig. 6c). In alkaline electrolytes, step I ($^*O_2 + 2H_2O + 4e^- \rightarrow OOH^* + H_2O + OH^- + 3e^-$) and step III ($^*O + H_2O + 2OH^- + 2e^- \rightarrow OH^* + 3OH^- + e^-$) are referred to as PCET steps and often considered the rate-determining steps, RDS. Therefore, enhancing proton supply and electron transfer is crucial for reducing the reaction barriers in the PCET process. Fig. 6d shows the Gibbs free energy plots of CoT-sp^{2}C-P-COF-COOH and CoT-sp^{2}C-P-COF for the ORR pathways. When U = 0 V, the free energy plots of CoT-sp^{2}C-P-COF-COOH and CoT-sp^{2}C-P-COF exhibit similar downslope energy paths, suggesting that this is a spontaneous exothermic process (Fig. 6e). When the potential increases to 1.23 V (Fig. 6f), CoT-sp^{2}C-P-COF-COOH demonstrated a lower activation energy of 0.24 eV in RDS (step I), which is significantly lower than that of CoT-sp^{2}C-P-COF (0.67 eV). Furthermore, analysis of the free energy diagram at U = 1.23 V reveals that the ΔG of step III on CoT-sp^{2}C-P-COF-COOH remains still lower than that of CoT-sp^{2}C-P-COF, demonstrating that the hydrophilic carboxyl groups synergistically facilitate both (PCET) steps.

3. Conclusion

In conclusion, we successfully synthesized CoT-sp^{2}C-P-COF-COOH using a simple post-synthetic method. Based on the enriched carboxyl functional groups incorporated in the pores, CoT-sp^{2}C-P-COF-COOH not only has good hydrophilicity but also enables continuous electron extraction and fast proton transport. Importantly, CoT-sp^{2}C-P-COF-COOH exhibited an outstanding half-wave potential of 0.823 V (*vs.* RHE), making it one of the most efficient of reported COF-based electrocatalysts. Besides, the electrochemical performance of the CoT-sp^{2}C-P-COF-COOH based zinc–air battery displayed a peak power density of 121.8 mW cm^{-2} and remarkable long-term cycling

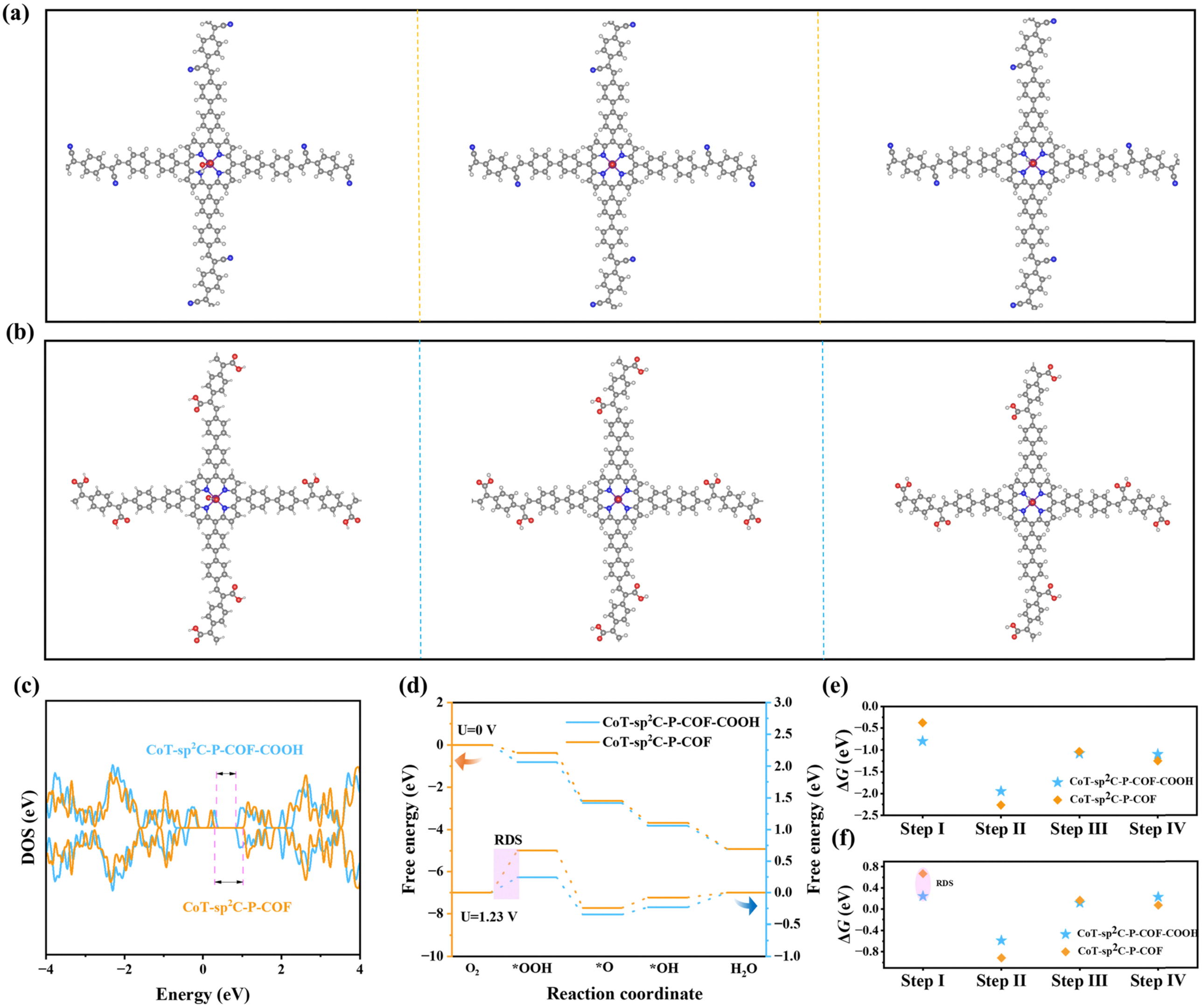

Fig. 6 The geometry of (a) CoT-sp^{2}C-P-COF, and (b) CoT-sp^{2}C-P-COF-COOH at the Co–N$_4$ active center of the intermediate OOH*, O*, and OH* desorption steps. C, N, Co, O, and H atoms are presented by dark gray, blue, violet, red and gray. (c) Calculated density of states (DOS) for CoT-sp^{2}C-P-COF and CoT-sp^{2}C-P-COF-COOH. (d) Gibbs free energy diagrams of CoT-sp^{2}C-P-COF and CoT-sp^{2}C-P-COF-COOH for the ORR at U = 0 V and U = 1.23 V. (e) and (f) ΔG of the basic steps in the ORR process at U = 0 V and U = 1.23 V, respectively.

durability. Results from both experimental and theoretical investigations demonstrated that CoT-sp^{2}C-P-COF-COOH binds O_2 more efficiently than CoT-sp^{2}C-P-COF, which contributes to the improvement of the adsorption of intermediates and electron transfer efficiency, thus accelerating the ORR kinetics and PCET steps. Overall, this study not only offers a facile strategy for utilizing substituents to alter the electronic structure and hydrophilic properties of COF catalysts for enhanced ORR, but also confirms their immense potential in electrocatalysis and energy conversion applications.

4. Experimental section

4.1. Materials

All reagents were purchased from commercial suppliers and were used directly without further purification unless otherwise stated (pyrrole was freshly distilled before use). All solvents used in these experiments were reagent grade. Carbon black (CB, acetylene, 50% compressed, 99.9+%) was purchased from Alfa.

4.2. Synthesis of T-sp^{2}C-P-COF

A mixture comprising 4-CHO-TBPP (32.96 mg, 0.032 mmol), PDAN (10.1 mg, 0.065 mmol) and TBAH (1.0 M, 0.2 mL) was charged into mesitylene/dioxane (1/1: v/v, 2 mL) within a 10 mL Pyrex tube. Subsequently, the tube was sonicated for 15 minutes, then quickly frozen in liquid nitrogen and degassed through three freeze pump-thaw cycles. Finally, the Pyrex tube was vacuum-sealed and then heated at 120 °C for 72 h. After cooling, the precipitate was collected *via* filtration, and washed with DMF, H_2O and THF several times. The product was further purified by Soxhlet extraction with THF for 24 h. The product

T-sp^{2}C-P-COF (34.82 mg) was prepared as a red-brown powder and then dried under vacuum conditions at 80 °C for 12 h.

4.3. Synthesis of CoT-sp^{2}C-P-COF

50 mg of T-sp^{2}C-P-COF, 200 mg (1.54 mmol) of $CoCl_2$ and 40 mL of CH_3OH were charged into a 100 mL round-bottom flask. The reaction mixture was heated at 80 °C for 12 h. Afterwards, the mixture was filtered and washed with CH_3OH several times. The product CoT-sp^{2}C-P-COF (59.77 mg) was obtained as a red-brown powder and then dried under vacuum conditions at 60 °C for 12 h.

4.4. Synthesis of CoT-sp^{2}C-P-COF-COOH

CoT-sp^{2}C-P-COF (50 mg), 10 M aqueous NaOH (10 ml) and ethanol (10 mL) were added into a 100 mL round-bottom flask. The reaction mixture was heated at 95 °C for 72 h. Subsequently, the mixture was brought to neutral pH by adding aqueous HCl (1.0 M) and filtered and washed with THF and water several times. The product CoT-sp^{2}C-P-COF-COOH (46.5 mg) was obtained as a red-brown powder and then dried under vacuum conditions at 60 °C for 12 h.

Author contributions

Yan-Fang Yao: writing – original draft, validation, methodology, investigation, formal analysis, data curation, conceptualization. Yun-Rui Lv: validation, formal analysis. Feng Li: validation, formal analysis. Xin-Yi Huang: validation, formal analysis. Si-Jing Huang: writing – review & editing, supervision. Xin-Yan Xiao: writing – review & editing, supervision. Hai-Yang Liu: writing – review & editing, supervision, resources, funding acquisition.

Conflicts of interest

There are no conflicts to declare.

Data availability

The authors declare that the data supporting the findings of this study are available within the paper and its ESI†.

Acknowledgements

We gratefully acknowledge financial support from the National Natural Science Foundation of China (No. 21671068, 21878115).

References

1 A. E. Thorarinsdottir, D. P. Erdosy, C. Costentin, J. A. Mason and D. G. Nocera, *Nat. Catal.*, 2023, **6**, 425–434.
2 D. G. Nocera, *J. Am. Chem. Soc.*, 2022, **144**, 1069–1081.
3 H. Stančin, H. Mikulčić, X. Wang and N. Duić, *Renewable Sustainable Energy Rev.*, 2020, **128**, 109927.
4 J. Zhang, T. Zhang, J. Ma, Z. Wang, J. Liu and X. Gong, *Carbon*, 2021, **172**, 556–568.
5 R. Ren, L. Yang, Z. Lin, X. Li, S. Zhang, T. Zheng, D. Wu, J. Wang, Z. Wei, W. Ding, N. Huang, M. Gu and Q. He, *J. Mater. Chem. A*, 2022, **10**, 22781–22790.
6 I. Staffell, D. Scamman, A. Velazquez Abad, P. Balcombe, P. E. Dodds, P. Ekins, N. Shah and K. R. Ward, *Energy Environ. Sci.*, 2019, **12**, 463–491.
7 W. E. Mustain, M. Chatenet, M. Page and Y. S. Kim, *Energy Environ. Sci.*, 2020, **13**, 2805–2838.
8 N. T. Nesbitt, T. Burdyny, H. Simonson, D. Salvatore, D. Bohra, R. Kas and W. A. Smith, *ACS Catal.*, 2020, **10**, 14093–14106.
9 L. Meng, S. Niu, Z. Wei, X. Qin, F. Naseem and W. Wei, *Appl. Catal., B*, 2025, **367**, 125080.
10 C. T. Carver, B. D. Matson and J. M. Mayer, *J. Am. Chem. Soc.*, 2012, **134**, 5444–5447.
11 T. Wang, Y. Zhang, B. Huang, B. Cai, R. R. Rao, L. Giordano, S. Sun and Y. Shao-Horn, *Nat. Catal.*, 2021, **4**, 753–762.
12 E. C. M. Tse, C. J. Barile, N. A. Kirchschlager, Y. Li, J. P. Gewargis, S. C. Zimmerman, A. Hosseini and A. A. Gewirth, *Nat. Mater.*, 2016, **15**, 754–759.
13 L. Li, X. Lv, Y. Xue, H. Shao, G. Zheng and Q. Han, *Angew. Chem., Int. Ed.*, 2024, **63**, e202320218.
14 S. Tao, L. Zhai, A. D. Dinga Wonanke, M. A. Addicoat, Q. Jiang and D. Jiang, *Nat. Commun.*, 2020, **11**, 1981.
15 A. P. Côté, A. I. Benin, N. W. Ockwig, M. O'Keeffe, A. J. Matzger and O. M. Yaghi, *Science*, 2005, **310**, 1166–1170.
16 D. Rodríguez-San-Miguel and F. Zamora, *Chem. Soc. Rev.*, 2019, **48**, 4375–4386.
17 J. Li, X. Jing, Q. Li, S. Li, X. Gao, X. Feng and B. Wang, *Chem. Soc. Rev.*, 2020, **49**, 3565–3604.
18 J. Tang, C. Su and Z. Shao, *Small Methods*, 2021, **5**, 2100945.
19 H. Chen, Q. Li, W. Yan, Z. Gu and J. Zhang, *Chem. Eng. J.*, 2020, **401**, 126149.
20 S. Jing, Z. Gu and J. Zhang, *J. Am. Chem. Soc.*, 2025, **147**, 8948–8958.
21 H. Chen, Z. Gu and J. Zhang, *J. Am. Chem. Soc.*, 2022, **144**, 7245–7252.
22 Z. Mei, G. Zhao, C. Xia, S. Cai, Q. Jing, X. Sheng, H. Wang, X. Zou, L. Wang, H. Guo and B. Y. Xia, *Angew. Chem., Int. Ed.*, 2023, **62**, e202303871.
23 J. Li, P. Liu, J. Yan, H. Huang and W. Song, *Adv. Sci.*, 2023, **10**, 2206165.
24 B. Luan, X. Chu, Y. Wang, X. Qiao, Y. Jiang and F. Zhang, *Adv. Mater.*, 2024, **36**, 2412653.
25 X. Li, S. Yang, X. Yang, S. Zheng, Q. Xu, G. Zeng and Z. Jiang, *ACS Catal.*, 2024, 17862–17870.
26 S. Bhunia, A. Peña-Duarte, H. Li, H. Li, M. F. Sanad, P. Saha, M. A. Addicoat, K. Sasaki, T. A. Strom, M. J. Yacamán, C. R. Cabrera, R. Seshadri, S. Bhattacharya, J. Brédas and L. Echegoyen, *ACS Nano*, 2023, **17**, 3492–3505.
27 X. Li, S. Yang, M. Liu, X. Yang, Q. Xu, G. Zeng and Z. Jiang, *Angew. Chem., Int. Ed.*, 2023, **62**, e202304356.
28 A. A. Gewirth, J. A. Varnell and A. M. DiAscro, *Chem. Rev.*, 2018, **118**, 2313–2339.
29 H. Qin, Y. Wang, B. Wang, X. Duan, H. Lei, X. Zhang, H. Zheng, W. Zhang and R. Cao, *J. Energy Chem.*, 2021, **53**, 77–81.

30 S. Huang, K. Chen and T. Li, *Coord. Chem. Rev.*, 2022, **464**, 214563.

31 B. Li, S. Zhang, X. Chen, C. Chen, Z. Xia and Q. Zhang, *Adv. Funct. Mater.*, 2019, **29**, 1901301.

32 S. Kandambeth, D. B. Shinde, M. K. Panda, B. Lukose, T. Heine and R. Banerjee, *Angew. Chem., Int. Ed.*, 2013, **52**, 13052–13056.

33 L. Jiao, W. Yang, G. Wan, R. Zhang, X. Zheng, H. Zhou, S. Yu and H. Jiang, *Angew. Chem., Int. Ed.*, 2020, **59**, 20589–20595.

34 H. Zhong, M. Wang, M. Ghorbani-Asl, J. Zhang, K. H. Ly, Z. Liao, G. Chen, Y. Wei, B. P. Biswal, E. Zschech, I. M. Weidinger, A. V. Krasheninnikov, R. Dong and X. Feng, *J. Am. Chem. Soc.*, 2021, **143**, 19992–20000.

35 Q. Zuo, G. Cheng and W. Luo, *Dalton Trans.*, 2017, **46**, 9344–9348.

36 S. Zheng, Y. Fu, X. Xu, Q. Xu and G. Zeng, *Angew. Chem., Int. Ed.*, 2025, e202503434.

37 X. Yang, Y. Fu, M. Liu, S. Zheng, X. Li, Q. Xu and G. Zeng, *Angew. Chem., Int. Ed.*, 2024, **63**, e202319247.

38 X. Yang, Q. An, X. Li, Y. Fu, S. Yang, M. Liu, Q. Xu and G. Zeng, *Nat. Commun.*, 2024, **15**, 1889.

39 R. Cheng, B. Ran, X. Zhang, Y. Han, X. Shao, H. Li and C. Fu, *Adv. Funct. Mater.*, 2024, **34**, 2406717.

40 C. Li, Z. Wang, Y. Jin, Z. Li, J. Jeon, S. Zhao, Y. Shao, F. Tang, W. Kim, R. Guan, J. Seo, Z. Lee, S. Lee and J. Baek, *Angew. Chem., Int. Ed.*, 2025, e202500336.

41 F. Wen, K. Xu, Y. Feng and N. Huang, *J. Am. Chem. Soc.*, 2024, **146**, 19680–19685.

42 H. Xu, Y. Wang, Y. Xu, Q. Wang, M. Zhuang, Q. Liao and K. Xi, *Angew. Chem., Int. Ed.*, 2024, **63**, e202408802.

43 X. Guan, H. Li, Y. Ma, M. Xue, Q. Fang, Y. Yan, V. Valtchev and S. Qiu, *Nat. Chem.*, 2019, **11**, 587–594.

44 S. Yang, W. Liu, Y. Zhang, X. Jia, J. Sun, C. Zhang and M. Liu, *J. Mater. Chem. A*, 2024, **12**, 28161–28169.

45 Z. You, B. Wang, Z. Zhao, Q. Zhang, W. Song, C. Zhang, X. Long and Y. Xia, *Adv. Mater.*, 2023, **35**, 2209129.

46 J. Yue, Y. Wang, X. Wu, P. Yang, Y. Ma, X. Liu and B. Tang, *Chem. Commun.*, 2021, **57**, 12619–12622.

47 J. X. Koh, K. Geng and D. Jiang, *Chem. Commun.*, 2021, **57**, 9418–9421.

48 W. Zhen, D. W. Kang, Y. Fan, Z. Wang, T. Germanas, G. T. Nash, Q. Shen, R. Leech, J. Li, G. S. Engel, R. R. Weichselbaum and W. Lin, *J. Am. Chem. Soc.*, 2024, **146**, 16609–16618.

49 H. Hao, F. Zhang, X. Wang, F. Huang, S. Chen and X. Lang, *Adv. Funct. Mater.*, 2025, **35**, 2419735.

50 H. Ma, M. Gu, M. Li, C. Gu, D. Zhu, G. Chen and Y. Dong, *Angew. Chem., Int. Ed.*, 2025, e202506509.

51 A. Kong, T. Yang, H. Yan, X. Chen, Y. Chen, F. Kang, Q. Zhang and R. Liu, *J. Am. Chem. Soc.*, 2025, **147**, 20855–20864.

52 J. Fang, Z. Fu, X. Chen, Y. Liu, F. Chen, Y. Wang, H. Li, Y. Yusran, K. Wang, V. Valtchev, S. Qiu, B. Zou and Q. Fang, *Angew. Chem., Int. Ed.*, 2023, **62**, e202304234.

53 Y. Zhang, X. Guan, Z. Meng and H. Jiang, *J. Am. Chem. Soc.*, 2025, **147**, 3776–3785.

54 Z. Yang, H. Chen, S. Wang, W. Guo, T. Wang, X. Suo, D. Jiang, X. Zhu, I. Popovs and S. Dai, *J. Am. Chem. Soc.*, 2020, **142**, 6856–6860.

55 R. Shi, L. Liu, Y. Lu, C. Wang, Y. Li, L. Li, Z. Yan and J. Chen, *Nat. Commun.*, 2020, **11**, 178.

56 X. Li, Y. Chu, S. Lu, L. Chen, L. Su, F. Lu, Z. Chen and X. Gao, *Chem. Eng. J.*, 2025, **505**, 159182.

57 W. Cheng, X. Zhao, H. Su, F. Tang, W. Che, H. Zhang and Q. Liu, *Nat. Energy*, 2019, **4**, 115–122.

58 Y. Wei, L. Zhao, Y. Liang, M. Yuan, Q. Wu, Z. Xue, X. Qiu and J. Zhang, *Chem. Eng. J.*, 2023, **476**, 146575.

59 J. Zhang, Y. Mou, W. Suo, S. Yang, J. Shen, H. Xu, Z. Zeng, R. Zhang, Z. Liang, Y. Wang, H. Zheng, J. Cao and R. Cao, *Adv. Funct. Mater.*, 2025, **35**, 2417621.

60 T. Chen, C. Hao, Z. Chen, J. Li, C. Lin, P. K. Shen and Z. Q. Tian, *Chem. Eng. J.*, 2025, **505**, 159449.